

We will release the metadata, crops, camera parameters, landmarks, and raw images from our dataset, as well as the data processing code, training code, FID evaluation code, and all trained models.

1. Supplementary

In this supplement, we first introduce *Unsplash-Pexels*, an extra large-pose face dataset to facilitate more future work (Sec. 1.1). We then discuss the limitations of our models (Sec. 1.2). We demonstrate that our models can eliminate the “seam” artifact in EG3D in Sec. 1.3.

We discuss the problem of the original FID of EG3D (Sec. 1.4). Then we illustrate the influence of the buggy tri-plane in Sec. 1.5. Next, we present our data processing pipeline (Sec. 1.6), followed by the details of pose density computation (Sec. 1.7) and the visualization of yaw and pitch angles (Sec. 1.8). We also introduce the divided EG3D model (Sec. 1.9) and provide examples from our *LFFF* dataset (Sec. 1.10). Furthermore, we present the distributions of semantic attributes (Sec. 1.11). Finally, we provide further visual results of StyleGAN2-ada (Sec. 1.12) and EG3D models (Sec. 1.13) trained on our datasets.

1.1. Unsplash-Pexels Dataset

Besides the images from the Flickr¹, we additionally collect 19,321 images from Unsplash² and Pexels³, and process them using the same image processing method as *LFFF*. We denote the obtained dataset as *Unsplash-Pexels* (see samples in Fig. 1). We combine *Unsplash-Pexels* with *FFHQ*, named *FFHQ+Unsplash-Pexels*.



Figure 1: Representative samples from *Unsplash-Pexels*.

We use the same training methods as E_{var1}^{Ours} , E_{var2}^{Ours} to train models on the *FFHQ+Unsplash-Pexels* dataset, and get models E_{var1}^{UspPex} , E_{var2}^{UspPex} .

However, most of the images in Unsplash and Pexels were taken by professional photographers and processed by image filters, while the images in Flickr were from everyday life scenes taken by Flickr users. As a result, although the images in *Unsplash-Pexels* are processed using

¹<https://www.flickr.com>

²<https://unsplash.com>

³<https://www.pexels.com>

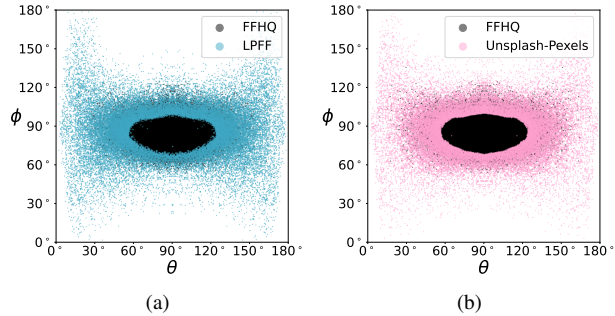


Figure 2: (a) *FFHQ+LFFF*. (b) *FFHQ+Unsplash-Pexels*.

the same method as *LFFF* and their camera distributions are similar (Fig. 2), the domain gap between *Unsplash-Pexels* and *FFHQ* would prevent the models trained on *FFHQ+Unsplash-Pexels* from generating view-consistent results.

As shown in Tab. 1 and 2, the models trained on *FFHQ+Unsplash-Pexels* present much worse performance in facial identity consistency and geometry consistency than the models trained on *FFHQ+LFFF*.

Thus we do not use *Unsplash-Pexels* as our training data, but propose this dataset to inspire and facilitate more work in the future.

model	$c_g = c_{avg}$ $c_r \sim \text{FFHQ}$	$c_g \sim \text{FFHQ}$ $c_r \sim \text{FFHQ}$	$c_g \sim \text{LFFF}$ $c_r \sim \text{FFHQ}$
E_{var1}^{UspPex}	0.800	0.788	0.774
E_{var1}^{Ours}	0.804	0.792	0.778
E_{var2}^{UspPex}	0.774	0.773	0.764
E_{var2}^{Ours}	0.789	0.784	0.771

Table 1: Quantitative evaluation of facial identity consistency (\uparrow).

model	$c_g = c_{avg}$ $c_r \sim \text{FFHQ}$	$c_g \sim \text{FFHQ}$ $c_r \sim \text{FFHQ}$	$c_g \sim \text{LFFF}$ $c_r \sim \text{FFHQ}$
E_{var1}^{UspPex}	0.135	0.135	0.142
E_{var1}^{Ours}	0.119	0.124	0.134
E_{var2}^{UspPex}	0.137	0.128	0.134
E_{var2}^{Ours}	0.117	0.122	0.131

Table 2: Quantitative evaluation of geometry consistency (\downarrow).

1.2. Limitations

Our models frequently generate “mask” artifacts at faces (Fig. 3 (a)), resulting in unsmooth cheek surfaces. We discover that this is due to improperly estimated densities. We

expect that future research incorporating genuine 3D face priors into the model will aid in resolving this issue. Our models tend to generate holes in faces when rendering eye-glasses because of lens refraction (Fig. 3 (b)). There are also fuzzy results or holes when rendering eyes from extreme camera postures (Fig. 3 (c)). Although our method can generate almost full-head 3D representations, the lack of data on the back of the head leads to incomplete head geometry (Fig. 3 (d)).

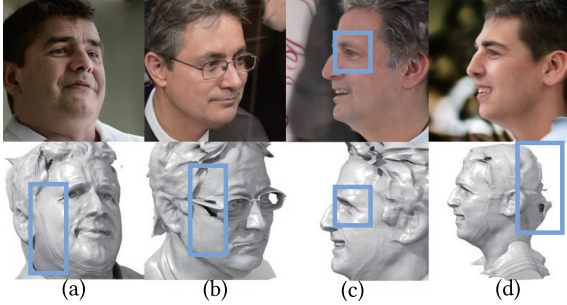


Figure 3: The limitations in our EG3D models (highlighted by blue boxes). (a) “Mask” artifacts. (b) Holes in faces when rendering eyeglasses. (c) Blurry results and holes in eyes. (d) Incomplete head geometry.

Inspired by EG3D, we use [3] to measure the probability of smiling against θ coordinate in $FFHQ+LPFF$. Fig. 4 shows that people typically smile when they are facing the camera, so the models trained on our dataset have the smile-posture entanglement.

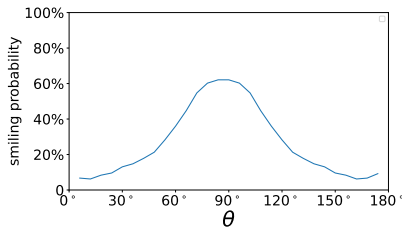


Figure 4: The probability of smiling against θ coordinate in $FFHQ+LPFF$. $\theta = 90^\circ$ stands for a frontal face.

1.3. Seam Artifacts Elimination

Fig. 5 presents the illustration of “seam” artifacts in the results of E_{var1}^{FFHQ} . Our model E_{var1}^{Ours} is trained without requiring any additional regularization loss or any data-rebalance strategy, and is free from the “seam” artifacts.

1.4. FID

During our evaluation of the FID for the EG3D model, we found that EG3D computes the FID by conditioning the model on c_g and then rendering results from $c_r = c_g$. In this

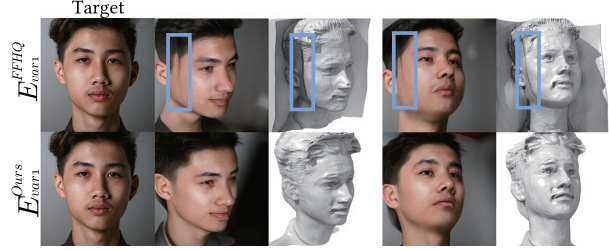


Figure 5: After employing PTI[2] GAN inversion, we use E_{var1}^{FFHQ} (Top) and E_{var1}^{Ours} (Bottom) to render novel views for the same target image. The “seam” artifacts are highlighted by blue boxes in the results of E_{var1}^{FFHQ} .

scenario, as shown in Fig. 6, the generator always perceives the true pose of the rendering camera, resulting in high-quality synthesized images. However, if we set $c_r \neq c_g$, the output exhibits artifacts and distortions. Consequently, the original FID measurement fails to accurately assess the quality of overall head geometry and multi-view rendering quality. Thus, we propose sampling c_r and c_g from different distributions.

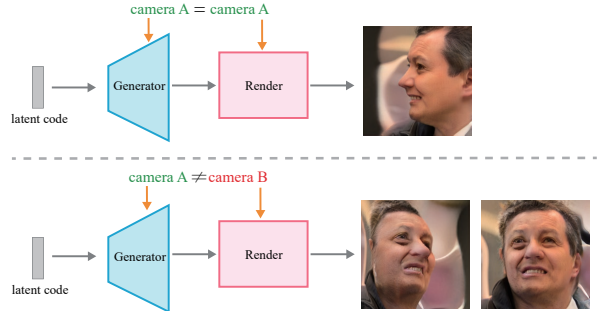


Figure 6: Visualization of the problem in the original FIDs measurement. When $c_r = c_g$ (Top), EG3D outputs good-quality results. When $c_r \neq c_g$ (Bottom), the results exhibit artifacts and distortion.

1.5. Buggy Tri-plane

In our evaluation results for the EG3D model, we found that there was an increased FID when computing $c_g = c_{avg}/c_r, c_r \sim FFHQ$, and we attributed this to the changed data variance and the buggy (XY, XZ, ZX) plane used in E_{var1}^{FFHQ} and E_{var2}^{FFHQ} . To provide a fairer comparison, we retrain the EG3D model using the (XY, XZ, ZY) plane (which was used in our models) on the $FFHQ$ dataset. Here, all the training parameters are identical to those of E_{var1}^{FFHQ} and E_{var1}^{Ours} . We denote the obtained model as $E_{var1-fixed}^{FFHQ}$. Then we compare the performance of E_{var1}^{FFHQ} , $E_{var1-fixed}^{FFHQ}$, and E_{var1}^{Ours} . Tab. 3, 4, and 5 show the comparison results, Figs. 7 presents the samples gener-

ated by $E_{var1-fixed}^{FFHQ}$.

The only difference between $E_{var1-fixed}^{FFHQ}$ and E_{var1}^{Ours} is their training datasets, but E_{var1}^{Ours} exhibits improvements in FID in most cases. When computing the FID of $c_r \sim FFHQ$, we obtain comparable results for $E_{var1-fixed}^{FFHQ}$ and E_{var1}^{Ours} . In terms of view-consistency, E_{var1}^{Ours} presents comparable performance to $E_{var1-fixed}^{FFHQ}$ in facial identity consistency, and shows improvements in geometry consistency across different sample strategies and datasets.

model	$c_g = c_{avg}$ $c_r \sim FFHQ$	$c_g \sim FFHQ$ $c_r \sim FFHQ$	$c_g \sim LPFF$ $c_r \sim FFHQ$
E_{var1}^{FFHQ}	0.771	0.768	0.760
$E_{var1-fixed}^{FFHQ}$	0.799	0.794	0.779
E_{var1}^{Ours}	0.804	0.792	0.778

Table 3: Quantitative evaluation of facial identity consistency (\uparrow).

model	$c_g = c_{avg}$ $c_r \sim FFHQ$	$c_g \sim FFHQ$ $c_r \sim FFHQ$	$c_g \sim LPFF$ $c_r \sim FFHQ$
E_{var1}^{FFHQ}	0.134	0.133	0.159
$E_{var1-fixed}^{FFHQ}$	0.125	0.125	0.144
E_{var1}^{Ours}	0.119	0.124	0.134

Table 4: Quantitative evaluation of geometry consistency (\downarrow).

In sum, our *LPFF* dataset can help the EG3D model to achieve higher image quality on large pose data while not harming the performance on *FFHQ*, and achieve better geometry consistency.

1.6. Data Processing Pipeline

We present the comparison between the image processing pipelines of StyleGAN, EG3D, and ours in Fig. 15.

1.7. Pose Density Computation

We propose representing the 6DOF camera pose and computing the pose density using 2DOF θ and ϕ angles. Because all cameras in EG3D are assumed to be on a spherical surface with radius $r = 2.7$, camera positions are determined by θ and ϕ angles. To prevent faces from appearing outside the image region, the faces are placed near the original point, just like the forward vector points (or look-at points). As a result, the camera’s forward direction is determined primarily by its position. We also ignore the upward direction of the cameras because all of the images are rotated and aligned in the preprocessing step using landmarks.

We define Cartesian coordinates as $[r \cos(\theta), r \sin(\theta) \cos(\phi), r \sin(\theta) \sin(\phi)]$ in this paper. Then



Figure 7: Image-shape pairs produced by $E_{var1-fixed}^{FFHQ}$. We apply truncation with $\psi = 0.8$.

we compute θ and ϕ for each camera and compute the pose density using kernel density estimation. When calculating this density, θ and ϕ are weighted similarly. Fig. 8 illustrates the visualization of θ and ϕ angles and their corresponding camera poses.

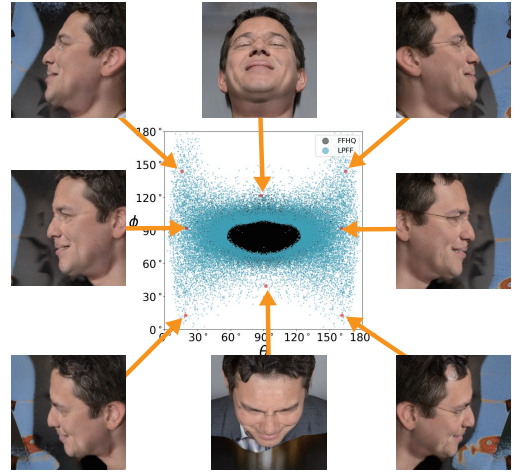


Figure 8: Visualization of camera poses.

1.8. The Yaw and Pitch Angles Visualization

We illustrate the distribution of yaw and pitch angles of the cameras in our dataset in Fig. 9.

1.9. EG3D Pipeline

We divide the EG3D model into three camera pose-dependent modules: Generator G , Renderer R , and Discriminator D , as shown in Fig. 16. The attribute correlations

model	$c_g = c_{avg}$ $c_r \sim \text{FFHQ}$	$c_g = c_{avg}$ $c_r \sim \text{LPFF}$	$c_g \sim \text{FFHQ}$ $c_r \sim \text{FFHQ}$	$c_g \sim \text{FFHQ}$ $c_r \sim \text{LPFF}$	$c_g \sim \text{LPFF}$ $c_r \sim \text{FFHQ}$	$c_g \sim \text{LPFF}$ $c_r \sim \text{LPFF}$	$c_g \sim \text{FFHQ}$ $c_r = c_g$	$c_g \sim \text{LPFF}$ $c_r = c_g$
E_{var1}^{FFHQ}	6.523	23.598	4.273	22.318	23.698	36.641	4.025	23.301
$E_{var1-fixed}^{\text{FFHQ}}$	7.689	23.962	6.572	22.537	22.567	33.063	6.102	25.115
E_{var1}^{Ours}	7.997	20.896	6.623	19.738	21.300	22.074	6.093	16.026

Table 5: FID (\downarrow) for EG3D generators that are trained on different datasets. We fixed the buggy tri-plane in E_{var1}^{FFHQ} , and re-trained the EG3D model using the (XY, XZ, ZY) plane on the *FFHQ* dataset. The obtained model is named as $E_{var1-fixed}^{\text{FFHQ}}$.

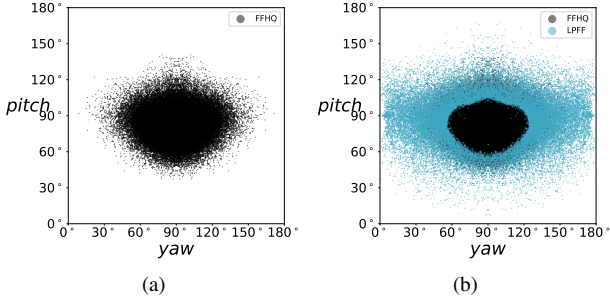


Figure 9: (a) *FFHQ*. (b) *FFHQ+LPFF*. The yaw and pitch distributions of LPFF and *FFHQ* datasets.

between pose and other semantic attributes in the dataset are faithfully modeled by feeding c_g into G . R and D are always fed with the same camera parameters, c_r . c_r help D ensure multi-view-consistent super resolution and direct R in how to render the final images from various camera views.

1.10. Image Samples from *LPFF* Dataset

As shown in Fig. 14, we present the image samples from our *LPFF* dataset. We used the official API from Flickr to obtain image metadata (including URLs) by searching portrait-related keywords (e.g., “portrait”, “people”), all images are under CC-BY-2.0⁴, Public-Domain-Mark-1.0⁵, CC-BY-SA-2.0⁶, or CC0-1.0⁷ licenses. Because the *FFHQ* dataset includes metadata for its photos (including copyright information and URLs), we remove the raw image when the *FFHQ* metadata already includes the raw image’s photo URL. The non-portrait images were removed by face detectors (Dlib and face alignment), while low-resolution images were filtered out automatically.

The images in the *LPFF* dataset are high-quality, large-pose, with variations on gender, age, race, expression, and lighting.

1.11. The Distributions of Attributes in *LPFF* Dataset

In Figures 10, 11, 12, and 13, we present comparisons of the distributions of different attributes detected by DeepFace [?], namely gender, race, age, and emotion, between our *LPFF* dataset and the *FFHQ* dataset. We notice that the *LPFF* has a higher proportion of males than *FFHQ*, possibly due to the difficulty in identifying females with long hair at large poses. However, based on the results presented in the main paper, this has little impact on our models.

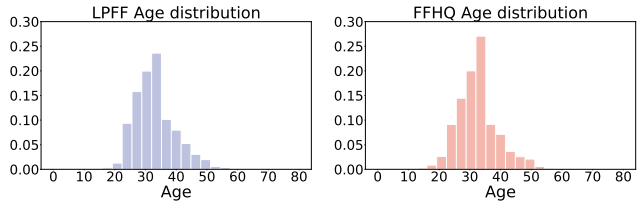


Figure 10: The age distributions of *LPFF* and *FFHQ* datasets.

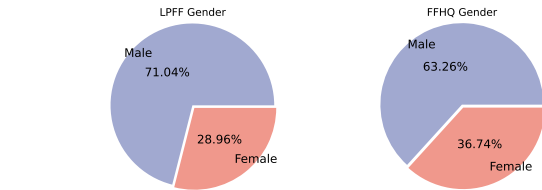


Figure 11: The gender distributions of *LPFF* and *FFHQ* datasets.

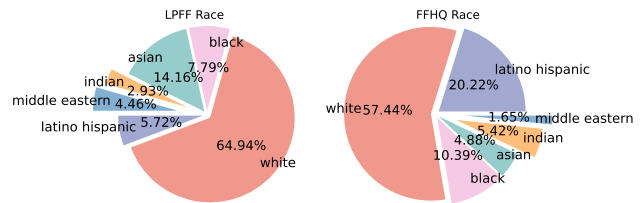


Figure 12: The race distributions of *LPFF* and *FFHQ* datasets.

⁴<https://creativecommons.org/licenses/by/2.0/>

⁵<https://creativecommons.org/publicdomain/mark/1.0/>

⁶<https://creativecommons.org/licenses/by-sa/2.0/>

⁷<https://creativecommons.org/publicdomain/zero/1.0/>

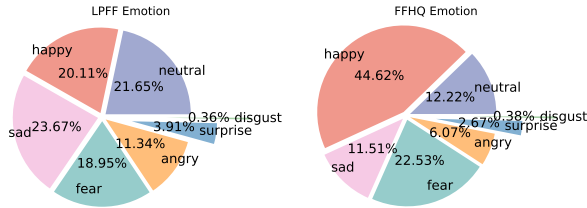


Figure 13: The emotion distributions of LPPF and FFHQ datasets.

1.12. Additional StyleGAN2-ada Results

1.12.1 StyleGAN2-ada Inversion Results

We present StyleGAN models’ large-pose data inversion results in Fig. 17 and 18. The testing images are collected from Unsplash and Pexels (out of the training datasets of all the models). The inversion is achieved by employing a 500-step latent code optimization to minimize the distance between the synthesis image and the target image. The optimization is performed in $W+$ latent space.

1.12.2 InterfaceGAN Pose Manipulation on StyleGAN Projection Results

After projecting the real large-pose images into the StyleGAN models’ latent space, we utilize the yaw angle editing directions to edit the obtained latent codes (Fig. 19 and 20).

1.12.3 InterfaceGAN Attribute Manipulation on StyleGAN Projection Results

After projecting the real large-pose images into the models’ latent space, we utilize the attribute editing directions to edit the obtained latent codes (Fig. 21 and 22).

We use the attribute classifiers provided by StyleGAN[1] to label the attribute scores of random latent codes, use InterfaceGAN to compute semantic boundaries for each model, and then use the boundaries to edit the projected latent codes.

1.13. Additional EG3D Results

1.13.1 EG3D Generation Results

We present the uncurated examples synthesized by models trained on our datasets in Fig. 23 and 24.

1.13.2 EG3D Extrapolation to Steep Camera Angles

Fig. 26 shows the comparison results of the steep angle generation results of the EG3D models trained on different datasets.

1.13.3 EG3D Image Inversion Results

Fig. 27 and Fig. 28 show the results of EG3D multi-view image inversion. We use 500-step latent code optimization to fit four testing images of a single identity from FaceScape [4]. Then we render the obtained latent codes from four novel views. The optimization is performed in $W+$ space, and the generators are conditioned on the average camera parameters.

Fig. 31 and 32 show the additional results of EG3D single-view image inversion. We perform PTI [2] inversion to single-view testing images collected from Unsplash and Pexels. The pivot latent codes are obtained by performing a 250-step latent code optimization in $W+$ space, and the models are fine-tuned using a 350-step PTI optimization.

References

- [1] Tero Karras, Samuli Laine, and Timo Aila. A style-based generator architecture for generative adversarial networks. In *IEEE Conference on Computer Vision and Pattern Recognition, CVPR*, pages 4401–4410, 2019. 5
- [2] Daniel Roich, Ron Mokady, Amit H. Bermano, and Daniel Cohen-Or. Pivotal tuning for latent-based editing of real images. *ACM Trans. Graph.*, 42(1), 2022. 2, 5
- [3] WuJie1010. Facial-expression-recognition.pytorch. <https://github.com/WuJie1010/Facial-Expression-Recognition.Pytorch>. 2
- [4] Haotian Yang, Hao Zhu, Yanru Wang, Mingkai Huang, Qiu Shen, Ruigang Yang, and Xun Cao. Facescape: A large-scale high quality 3d face dataset and detailed riggable 3d face prediction. In *IEEE Conference on Computer Vision and Pattern Recognition, CVPR*, pages 598–607, 2020. 5



Figure 14: Random image samples from the *LPFF* dataset. The presented images are aligned using the EG3D image alignment functions, at 512^2 resolution.

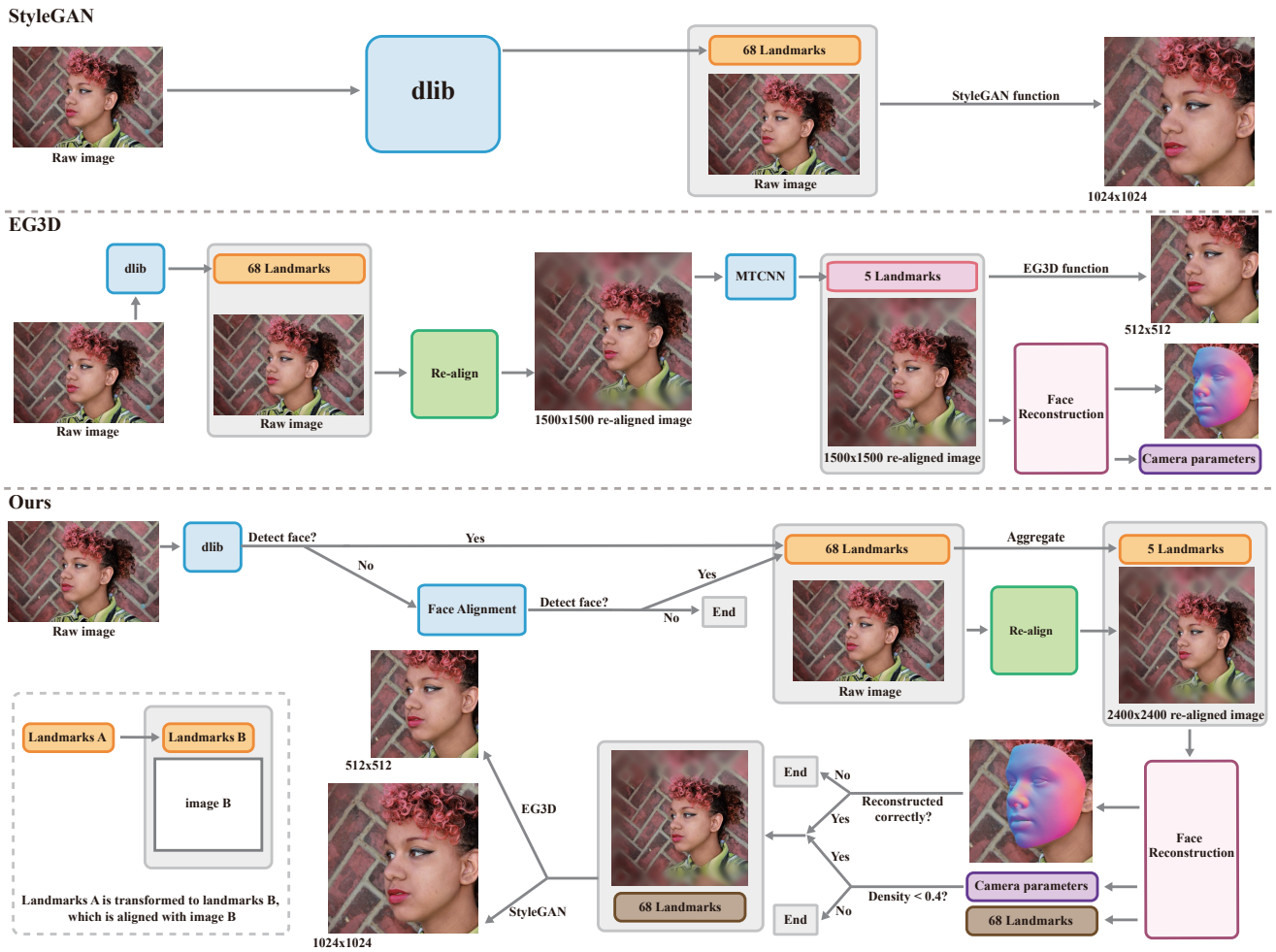


Figure 15: Image processing pipelines of StyleGAN, EG3D, and ours.

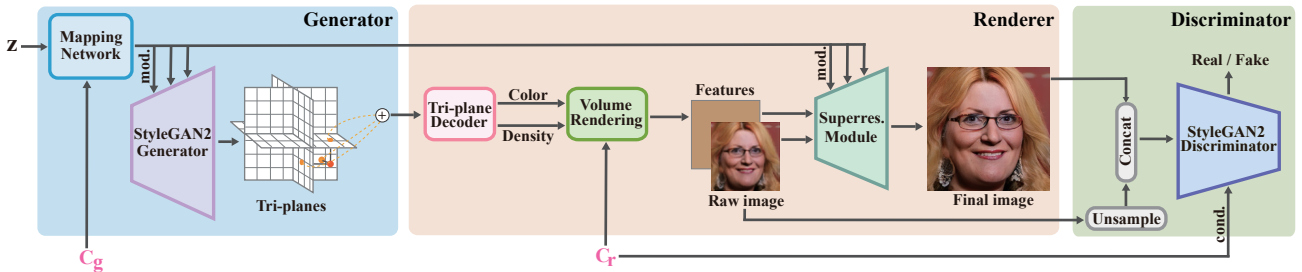


Figure 16: We split the EG3D model into three modules: Generator, Renderer, and Discriminator. We define the two kinds of camera parameters that are inputted into the EG3D modules as: c_g fed into the Generator is used to faithfully model the attribute correlations and will influence the face geometry and appearance. c_r guides the Renderer and the Discriminator to render the final images from different camera views while ensuring multi-view-consistent super resolution.



Figure 17: More qualitative comparison results for StyleGAN inversion.



Figure 18: More qualitative comparison results for StyleGAN projection.

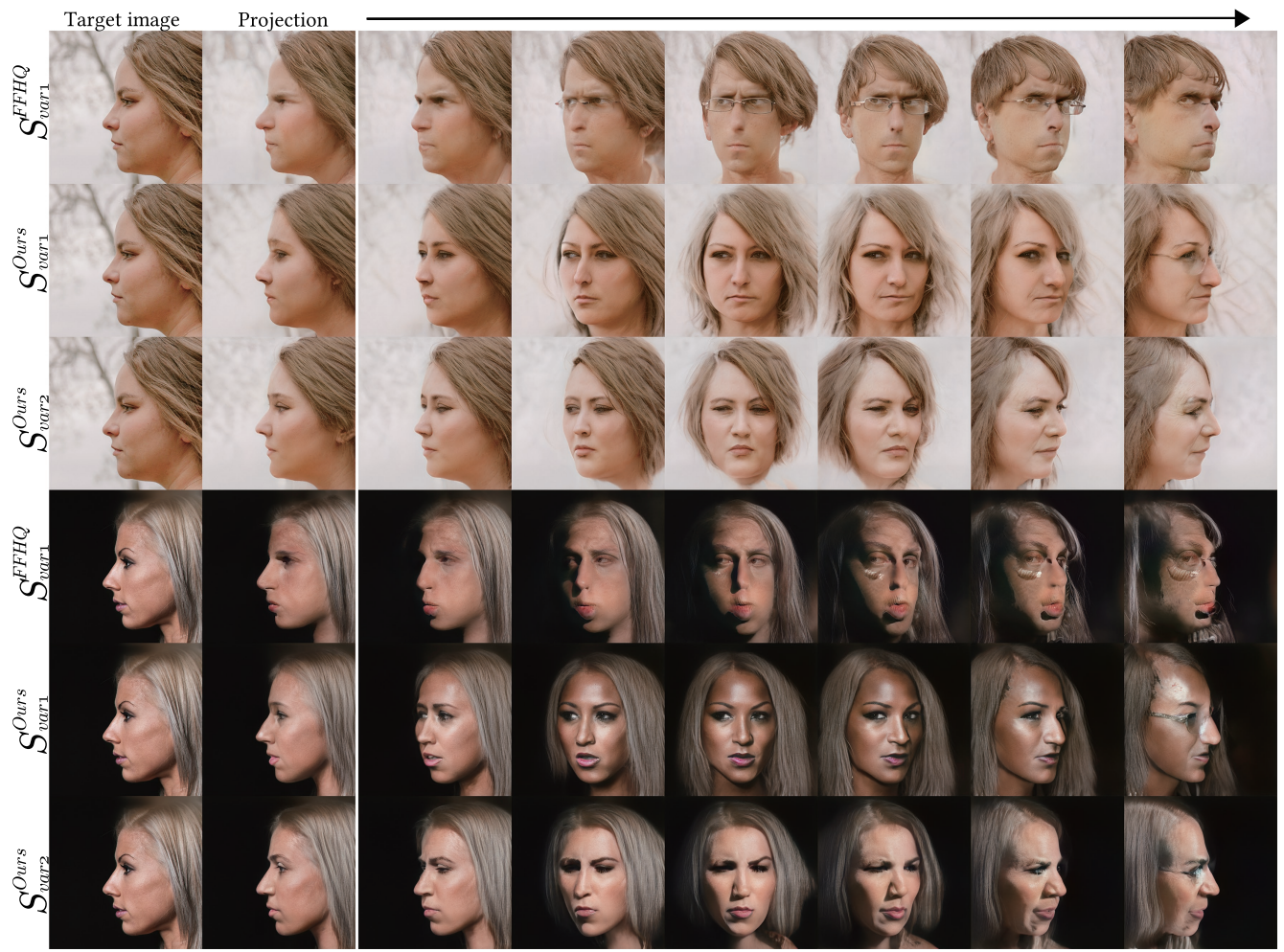


Figure 19: More qualitative comparison results for InterfaceGAN pose manipulation on StyleGAN inversion results.



Figure 20: More qualitative comparison results for InterfaceGAN pose manipulation on StyleGAN inversion results.

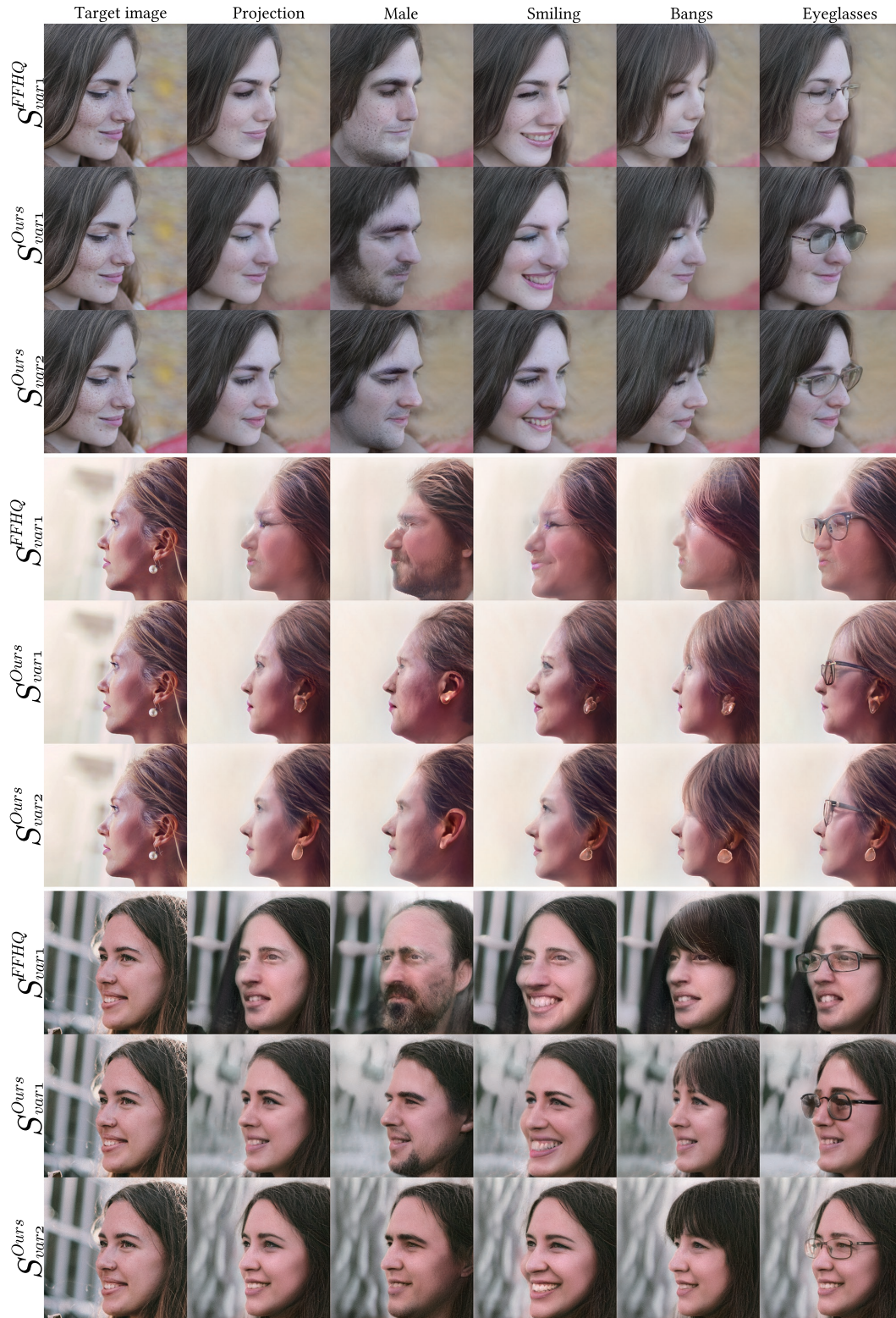


Figure 21: More qualitative comparison results for InterfaceGAN semantic attribute manipulation on StyleGAN inversion results.

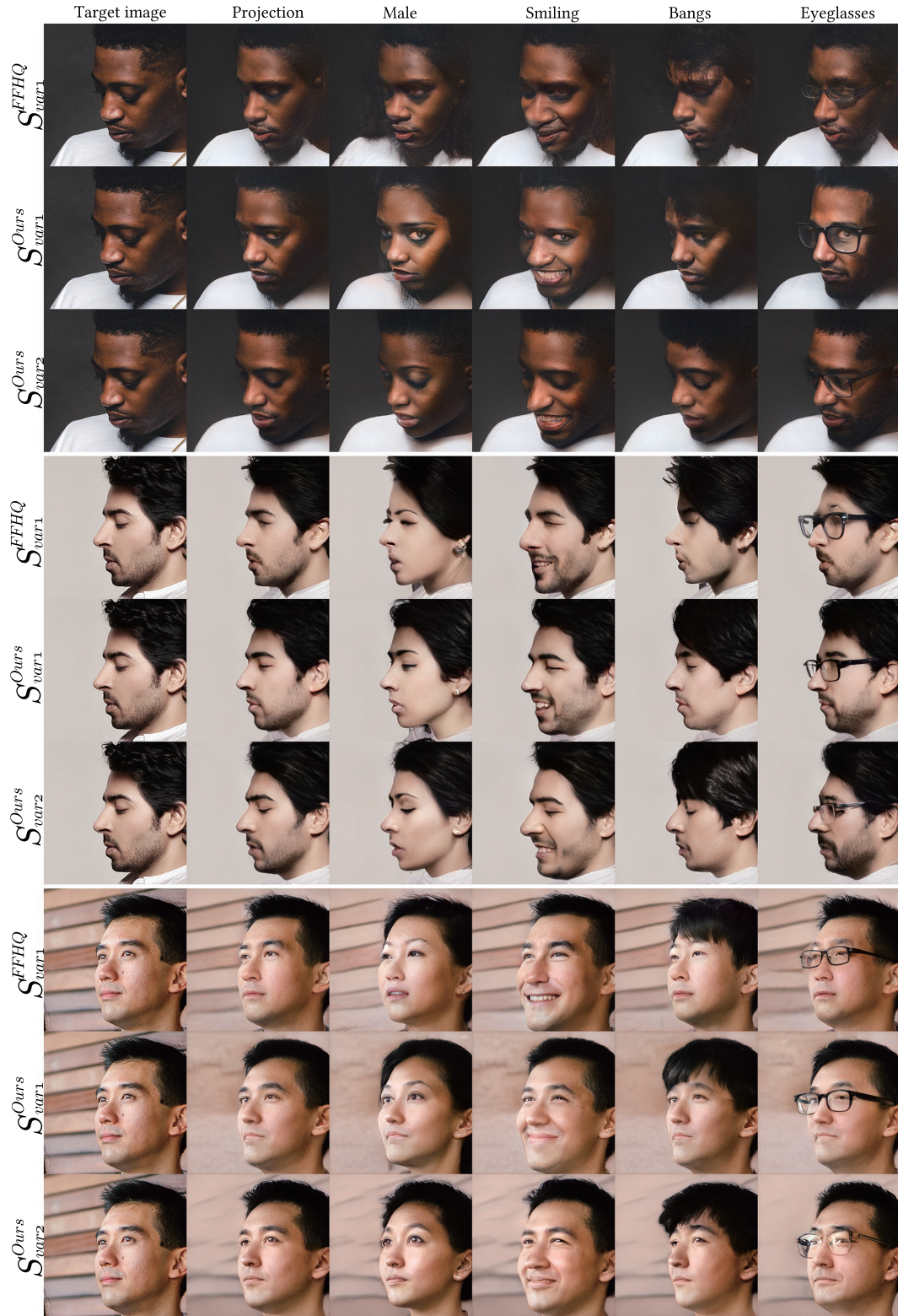


Figure 22: More qualitative comparison results for InterfaceGAN semantic attribute manipulation on StyleGAN inversion results.



Figure 23: Uncurated examples synthesized by E_{var1}^{Ours} , with truncation ($\psi = 0.6$).

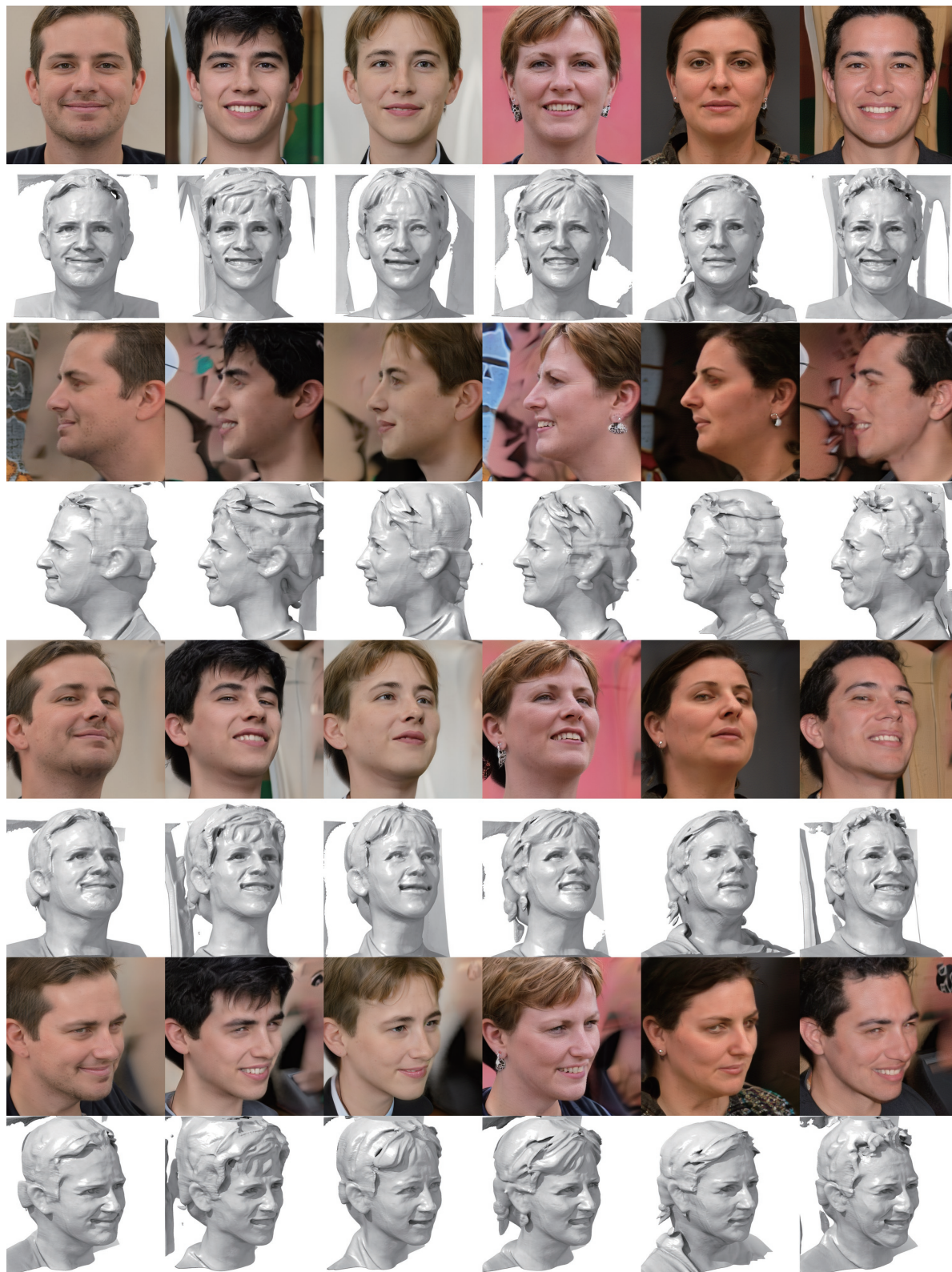


Figure 24: Uncurated examples synthesized by E_{var2}^{Ours} , with truncation ($\psi = 0.6$).



Figure 25: Extrapolation to steep pitch angles, with truncation ($\psi = 0.7$).

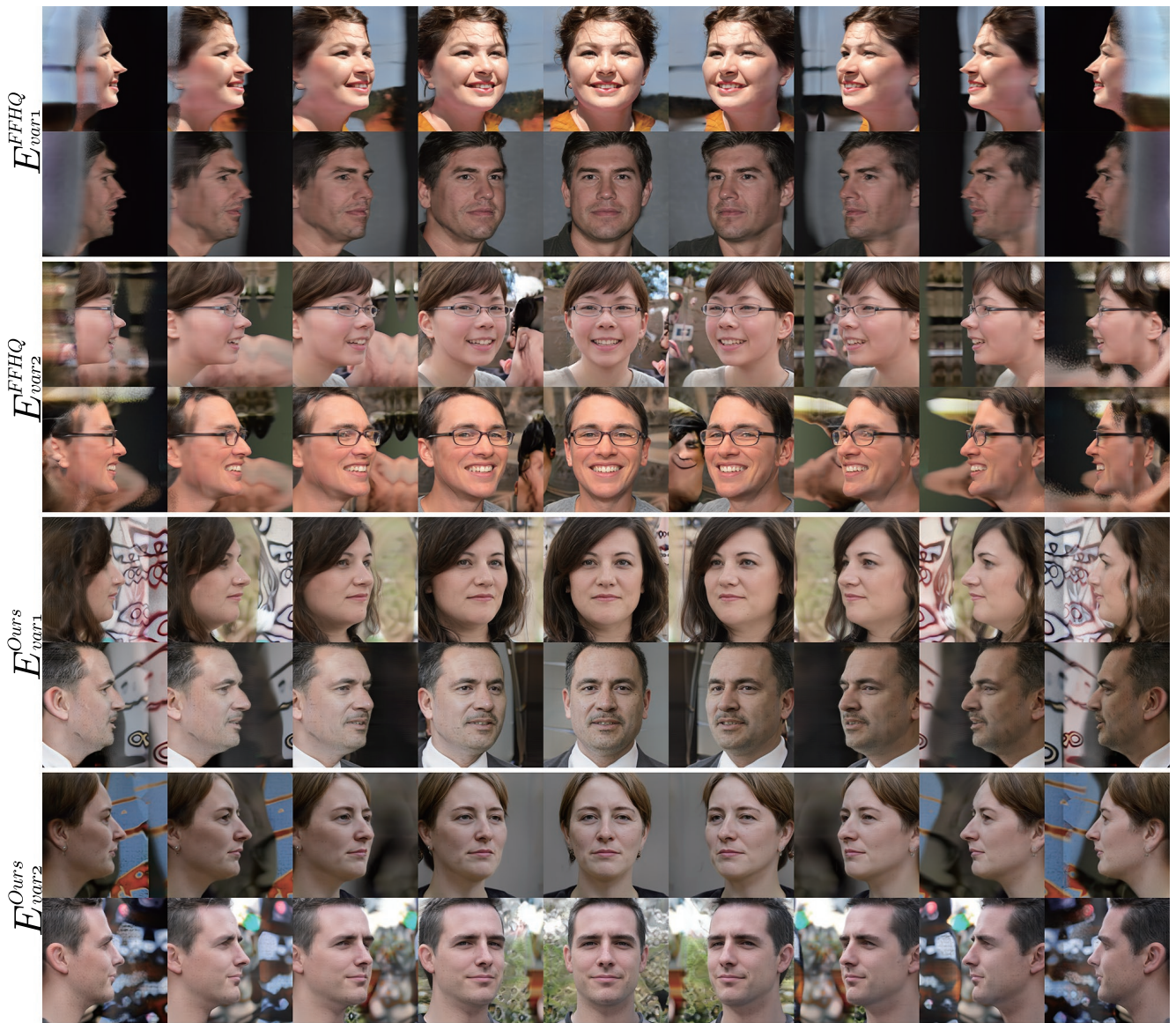


Figure 26: Extrapolation to steep yaw angles, with truncation ($\psi = 0.7$).

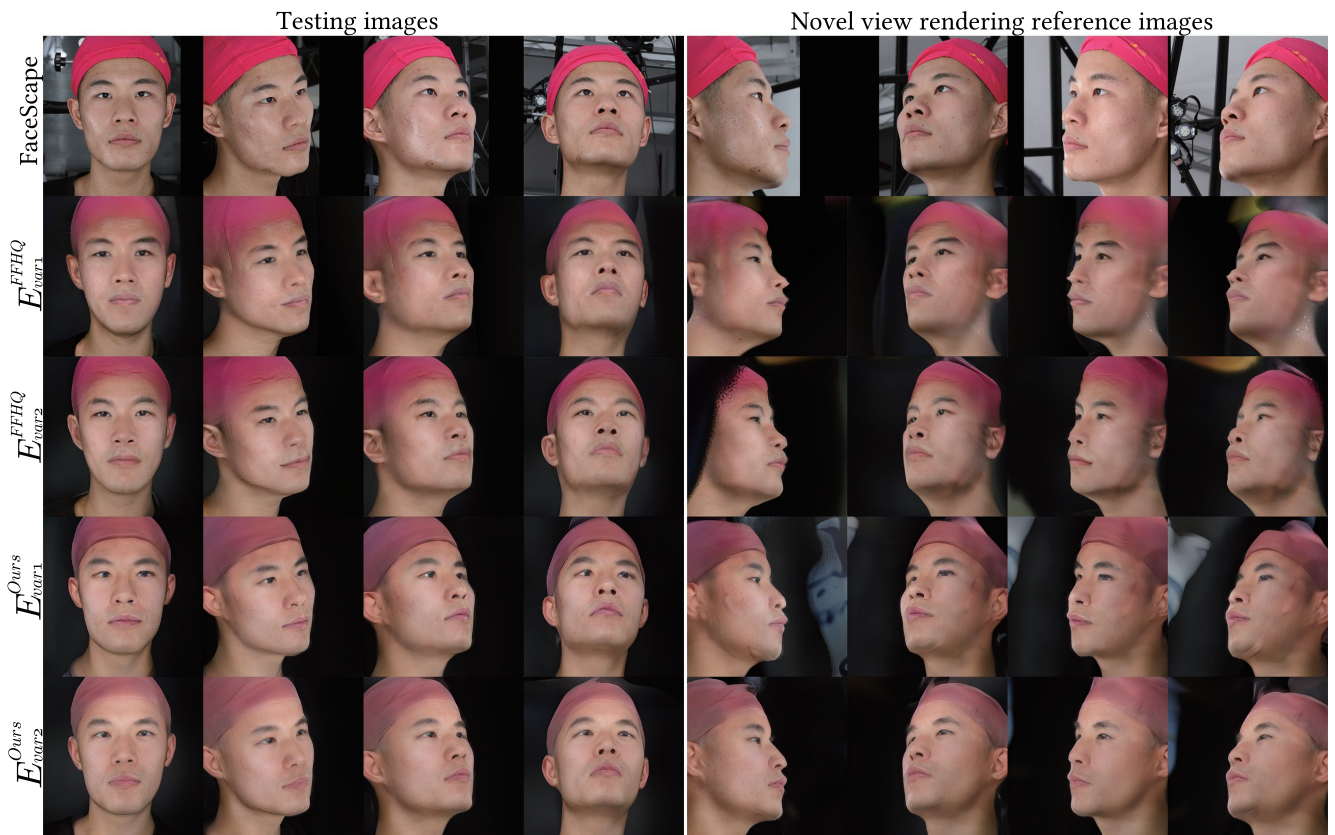


Figure 27: More EG3D multi-view image inversion results.

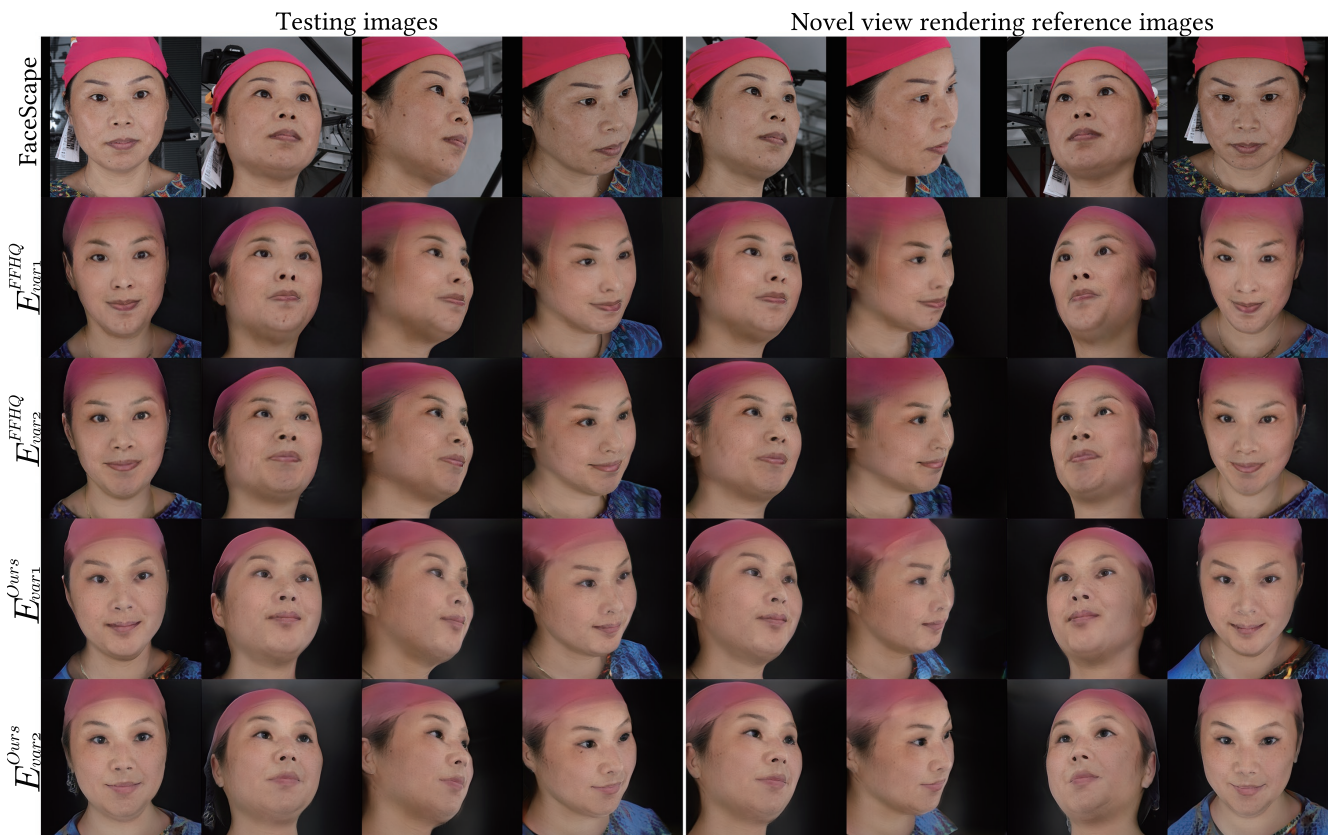


Figure 28: More EG3D multi-view image inversion results.

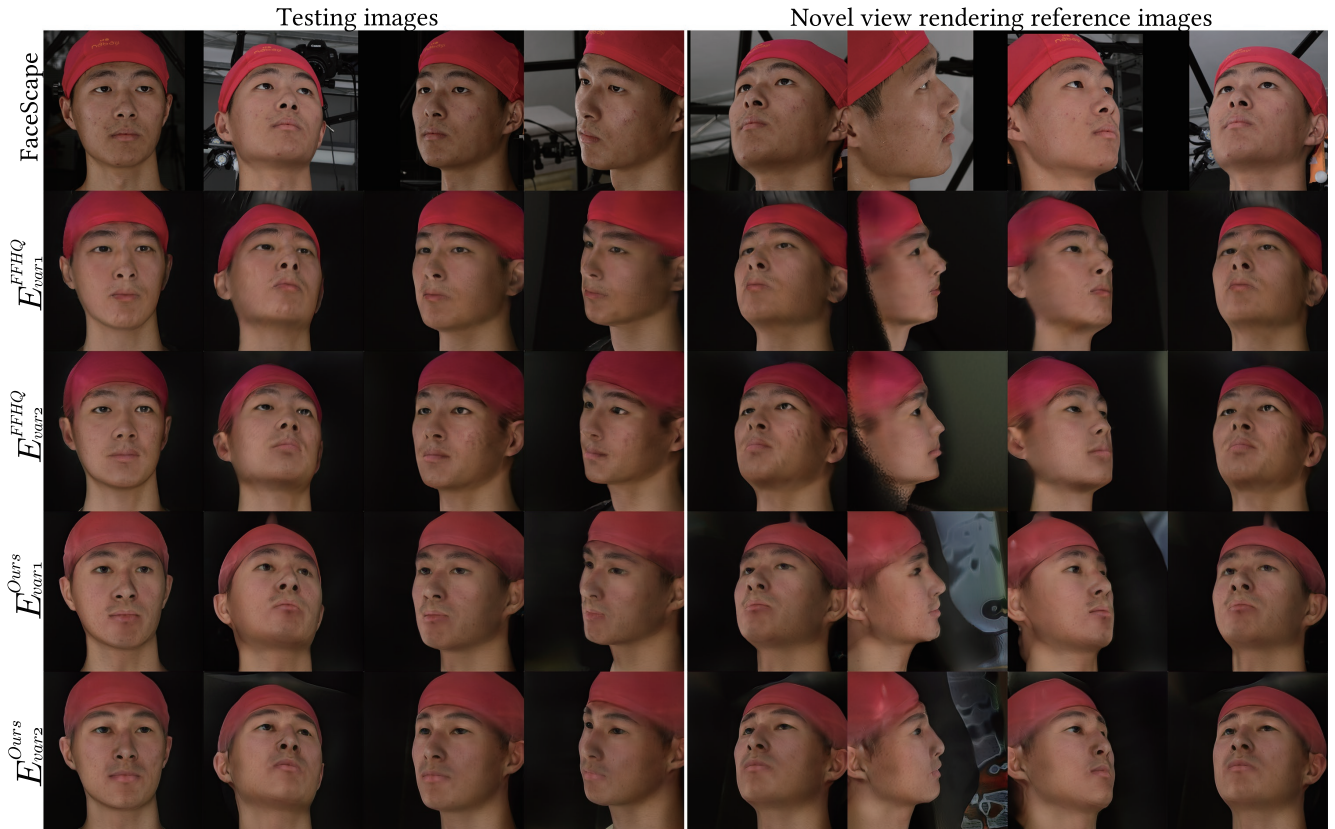


Figure 29: More EG3D multi-view image inversion results.

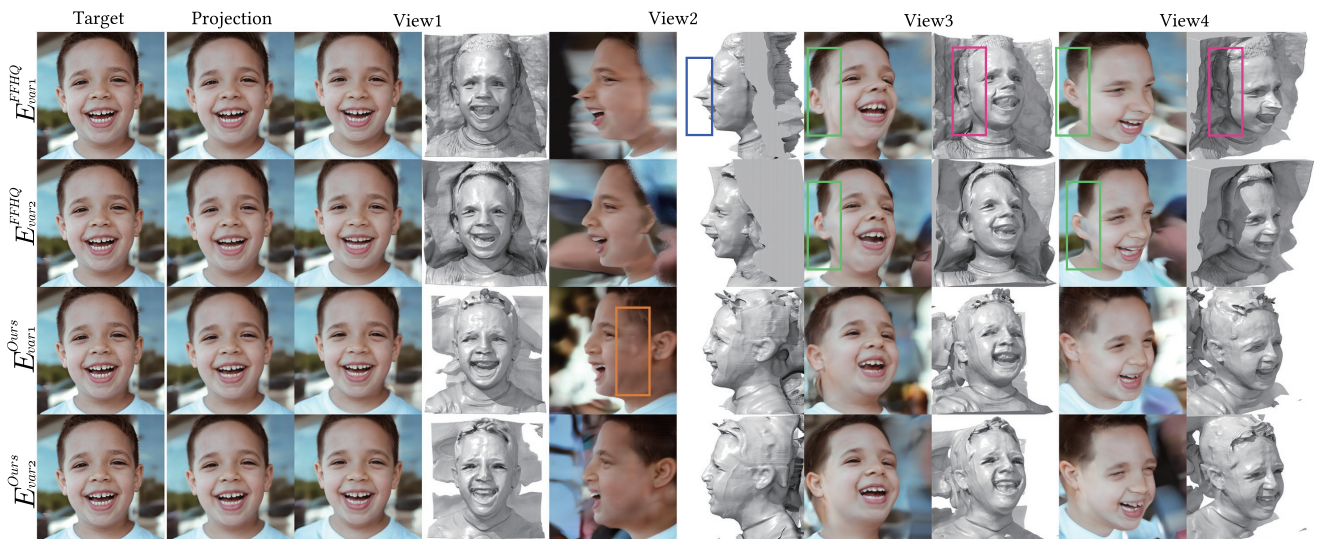


Figure 30: More EG3D single-view image inversion results. Due to the adhesion between the head and the background in E_{var1}^{FFHQ} and E_{var2}^{FFHQ} , ears are missing in View 2, and there are distortions in the ears and neck in Views 3 and 4 (highlighted by green boxes). E_{var1}^{FFHQ} also exhibits a pointed nose (highlighted by a blue box) and “seam” artifacts (highlighted by pink boxes). Additionally, compared to E_{var2}^{Ours} , there are some blurry skin artifacts present in E_{var1}^{Ours} (highlighted by an orange box).



Figure 31: More EG3D single-view image inversion results. E_{var1}^{FFHQ} has a hole on the nose (highlighted by blue boxes), while E_{var2}^{FFHQ} exhibits adhesion between the head and the background (adhesion by green boxes).

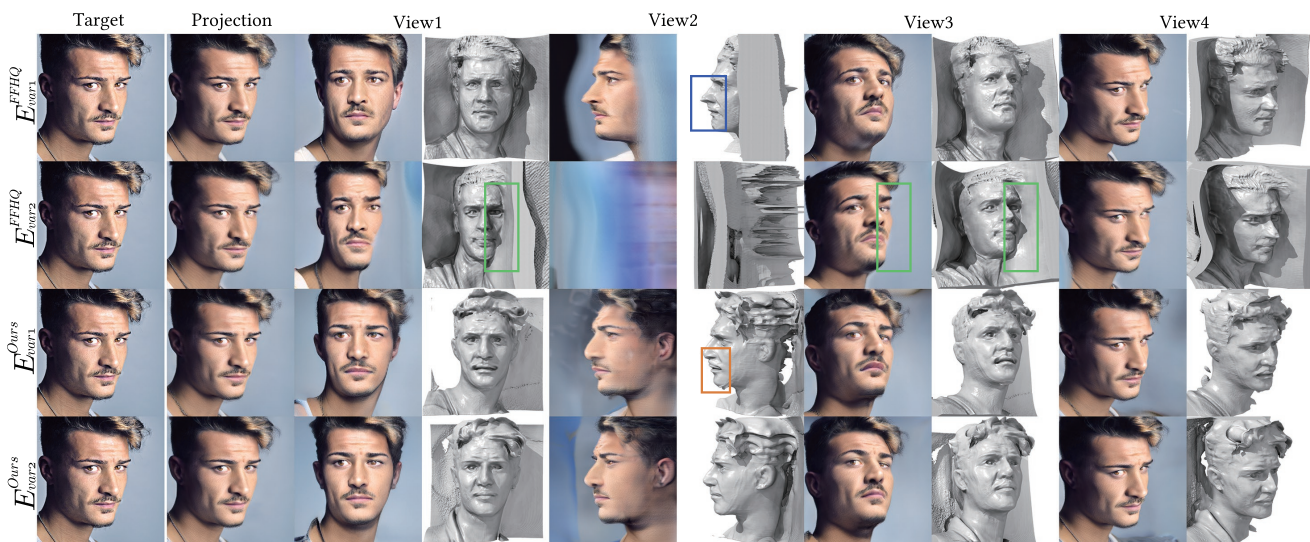


Figure 32: More EG3D single-view image inversion results. E_{var1}^{FFHQ} has a pointed nose (highlighted by a blue box). A severe distortion of background exists in E_{var2}^{FFHQ} (highlighted by green boxes). E_{Ours}^{var1} exhibits unnatural lips (highlighted by an orange box).

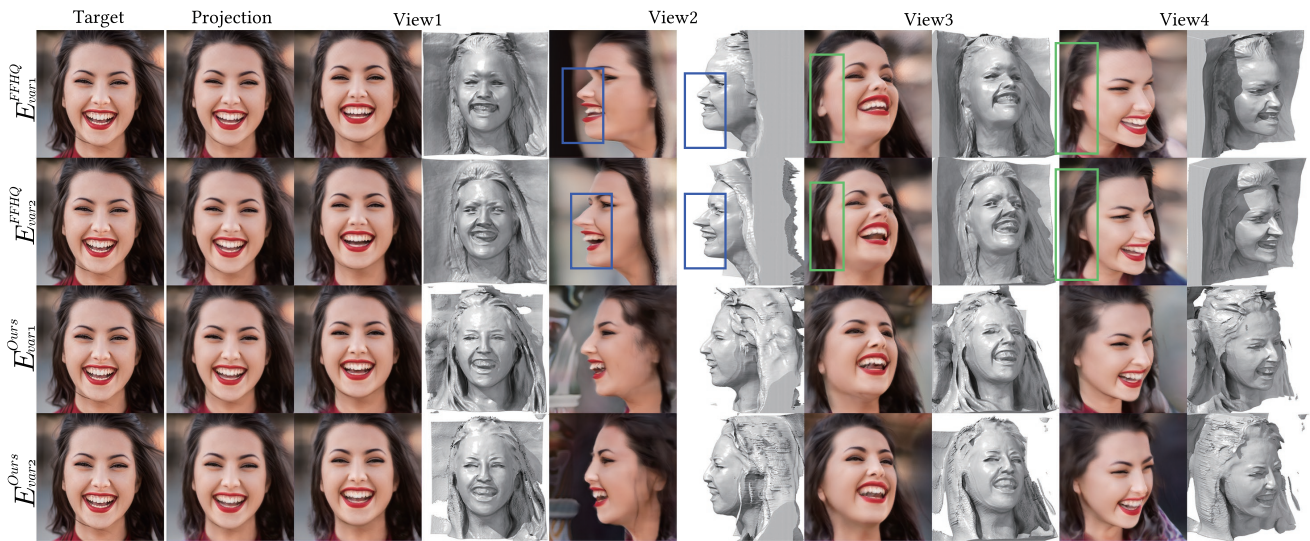


Figure 33: More EG3D single-view image inversion results. The results for E_{var1}^{FFHQ} and E_{var2}^{FFHQ} exhibit distorted faces (highlighted by blue boxes) and distorted ears and necks (highlighted by green boxes).